



**Cite this article:** Gonzalez-Rodriguez R, Granitzer P, Rumpf K, Coffey JL. 2018 New MRI contrast agents based on silicon nanotubes loaded with superparamagnetic iron oxide nanoparticles. *R. Soc. open sci.* **5**: 180697. <http://dx.doi.org/10.1098/rsos.180697>

Received: 14 May 2018

Accepted: 20 June 2018

**Subject Category:**

Chemistry

**Subject Areas:**

nanotechnology

**Keywords:**

silicon nanotubes, iron oxide, MRI, contrast agent

**Author for correspondence:**

Jeffery L. Coffey

e-mail: [j.coffey@tcu.edu](mailto:j.coffey@tcu.edu)

This article has been edited by the Royal Society of Chemistry, including the commissioning, peer review process and editorial aspects up to the point of acceptance.

Electronic supplementary material is available online at <https://dx.doi.org/10.6084/m9.figshare.c.4168718>.



# New MRI contrast agents based on silicon nanotubes loaded with superparamagnetic iron oxide nanoparticles

Roberto Gonzalez-Rodriguez<sup>1</sup>, Petra Granitzer<sup>2</sup>, Klemens Rumpf<sup>2</sup> and Jeffery L. Coffey<sup>1</sup>

<sup>1</sup>Department of Chemistry, Texas Christian University, Fort Worth, TX 76129 USA

<sup>2</sup>Institute of Physics, Karl-Franzens-University Graz, Universitaetsplatz 5, 8010 Graz, Austria

JLC, 0000-0003-0267-9646

This article describes the preparation and fundamental properties of a new possible material as a magnetic resonance imaging contrast agent based on the incorporation of preformed iron oxide (Fe<sub>3</sub>O<sub>4</sub>) nanocrystals into hollow silicon nanotubes (Si NTs). Specifically, superparamagnetic Fe<sub>3</sub>O<sub>4</sub> nanoparticles of two different average sizes (5 nm and 8 nm) were loaded into Si NTs of two different shell thicknesses (40 nm and 70 nm). To achieve proper aqueous solubility, the NTs were functionalized with an outer polyethylene glycol-diacid (600) moiety via an aminopropyl linkage. Relaxometry parameters  $r_1$  and  $r_2$  were measured, with the corresponding  $r_2/r_1$  ratios in phosphate buffered saline confirming the expected negative contrast agent behaviour for these materials. For a given nanocrystal size, the observed  $r_2$  values are found to be inversely proportional to NT wall thickness, thereby demonstrating the role of nanostructured silicon template on associated relaxometry properties.

## 1. Introduction

Superparamagnetic iron oxide nanoparticles (Fe<sub>3</sub>O<sub>4</sub> NPs) are the focus of extensive attention in areas such as catalysis [1], as well as biomedical applications such as cell labelling [2], biosensing [3], drug delivery [4], hyperthermia [5] and magnetic resonance imaging (MRI) [6]. In addition to their size-selective synthesis and useful fundamental magnetic properties, Fe<sub>3</sub>O<sub>4</sub> NPs have a very low toxicity and are biocompatible [7,8].

There is fundamental interest in the packaging of multiple magnetic nanocrystals in a well-defined host material, along with

the accompanying impact on physical properties [9–13]. One appealing option involves high surface area elemental silicon (Si) for this purpose, in the form of porous Si NPs [14,15] or silicon nanotubes (Si NTs) of a well-defined size and uniform structures. The NT length, along with the outer and inner diameter of the Si NTs, is in principle broadly tunable, with a wall thickness-dependent aqueous dissolution behaviour [16].

The characteristic quality of an MRI contrast agent is typically measured by the parameters of relaxivity  $r_1$  or  $r_2$ , which describe the ability of a given contrast agent to shorten the  $T_1$  or  $T_2$  relaxation time of water [17]. The most popular class of contrast agents in current use involves Gd-complex based  $T_1$  MRI contrast agents, with extensive development of nanoparticulate  $T_1$  contrast agents containing  $Gd^{3+}$  or  $Mn^{2+}$  ions intensively pursued in recent years [18]. However, toxicity problems still persist in these NP-based  $T_1$  contrast agents, thereby motivating additional studies towards the establishment of new alternatives. Of possible choices,  $Fe_3O_4$  offers a superior biocompatibility relative to the above gadolinium-based materials [19].  $Fe_3O_4$  MRI contrast agents are considered a negative contrast agent (or  $r_2$  weighted), with the possible enhancement often determined by several factors such as: (i) NP size; (ii) composition; (iii) surface coating; and (iv) synergistic magnetic effects arising from the presence of multiple superparamagnetic  $Fe_3O_4$  NP centres in a relatively small volume [20].

For MRI applications,  $Fe_3O_4$  NPs have been functionalized with different surface moieties to increase solubility [21]. The local concentration of  $Fe_3O_4$  in solution has also been increased by the assembly of other structures such as  $Fe_3O_4$  nanorods and clusters of individual  $Fe_3O_4$  NPs [22,23]. However, these clusters often lack uniformity and a well-defined three-dimensional structure. There is one report of  $Fe_3O_4$  NPs formed in carbon NTs [24]. Since the  $Fe_3O_4$  NPs are formed *in situ* inside the NTs, the  $Fe_3O_4$  nanostructures do not have a uniform particle size distribution [25]. To our knowledge, there are no reports of Si NTs loaded with  $Fe_3O_4$  NPs for MRI applications.

In this article, we describe loading processes for incorporating  $Fe_3O_4$  NPs into SiNTs, routes to surface modification of such loaded NTs for proper solubility, and the relaxivity properties of these  $Fe_3O_4$  NP-loaded Si NTs. We selected Si NTs of well-defined thickness (40 nm and 70 nm) that will not degrade during the timescale of the relaxivity measurements. To examine the role of  $Fe_3O_4$  nanocrystal size on loading and associated properties, we use NPs of both 5 nm and 8 nm diameter for this purpose. These experiments complement our earlier experiments involving investigations of the fundamental magnetic properties (blocking temperature, temperature-dependent coercivity) of new materials potentially useful as an MRI contrast agent based on  $Fe_3O_4$  NPs loaded into silicon nanostructures [26].

## 2. Material and methods

### 2.1. Iron oxide nanoparticles

The  $Fe_3O_4$  NPs used here were fabricated using a well-known route involving high temperature decomposition of a suitable molecular iron precursor. Further details regarding the fabrication process of these NPs can be found in previous publications [27].

### 2.2. Silicon nanotubes

Si NTs were fabricated by a sacrificial template method reported previously by our research group [16]. In general terms, it involves the initial formation of ZnO nanowire array (NWA) templates on a substrate (such as silicon wafers or F-doped tin oxide (FTO) glass), followed by Si deposition (540°C for 40 nm shell thickness Si NTs, 580°C for 70 nm shell thickness) and subsequent template removal by an  $NH_3/HCl$  etch under a helium atmosphere at 400°C. ZnO NWA templates were prepared on a given substrate (FTO or Si) that were previously seeded with ZnO nanocrystals (according to a previously described procedure) by placing in a mixture (1:1 v:v) of 0.03 M  $Zn(NO_3)_2$  and 0.03 M hexamethylenetetramine at 92°C for 9 h. Polyethylenimine (100  $\mu$ l, branched, low molecular weight, Aldrich) was added into 100 ml of ZnO growth solution. A given ZnO NWA sample was inserted into a quartz tube reactor and Si deposition on the ZnO NWA was achieved through the use of diluted silane (20 sccm, 0.5% in He) mixed with He carrier gas (200 sccm) that was passed through a furnace. These Si-coated ZnO NW samples were then placed in another quartz reactor and heated to 450°C;  $NH_4Cl$  was loaded in an alumina boat located

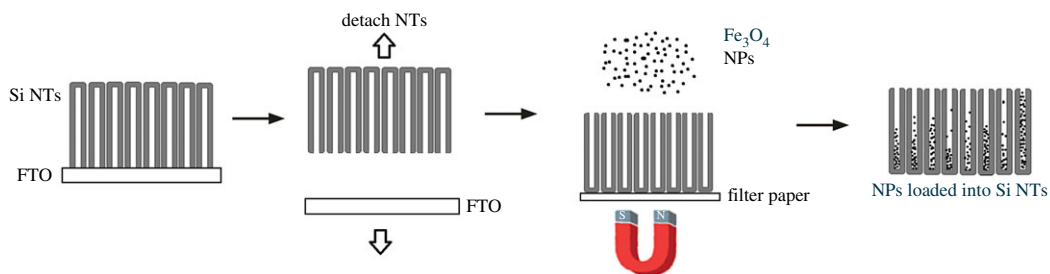


**Figure 1.** Loading process of  $\text{Fe}_3\text{O}_4$  NPs into silicon nanotubes (Si NTs). Si NT arrays are physically detached from their substrate; the film is then inverted and exposed to a solution of  $\text{Fe}_3\text{O}_4$  NPs with a bar magnet underneath.

upstream and heated to  $350^\circ\text{C}$ . The gaseous etchant was transported via He gas downstream (170 sccm) to the furnace for 1 h for removal of the ZnO NWA template.

### 2.3. Loading of $\text{Fe}_3\text{O}_4$ NPs into silicon nanotubes

The process for loading  $\text{Fe}_3\text{O}_4$  NPs into these NTs is illustrated in figure 1. This is readily achieved by initial physical removal of the Si NT film from the underlying substrate (such as FTO glass) and placing it face down on top of an Nd magnet with a piece of filter paper in between.  $\text{Fe}_3\text{O}_4$  NPs (oleic acid terminated, hexane solution) at a concentration of  $7\text{ mg ml}^{-1}$  are added dropwise, followed by rinsing the infiltrated sample with acetone several times and allowed to air dry.

### 2.4. Ferrozine assay

A Ferrozine assay was used to determine the concentration of iron [28]. This assay consists of taking a  $400\ \mu\text{l}$  solution containing a known mass of Si NTs loaded with  $\text{Fe}_3\text{O}_4$  NPs. This solution is then mixed with  $400\ \mu\text{l}$  of 12 M HCl and allowed to sit for 1 h, this solution is mixed with  $400\ \mu\text{l}$  of 12 M NaOH to neutralize the solution, followed by addition of  $96\ \mu\text{l}$  of 2.8 M  $\text{HONH}_2$  in 4 M HCl, followed by a waiting period of 1 h. Ammonium acetate ( $40\ \mu\text{l}$  10 M) is then added, followed by  $240\ \mu\text{l}$  of 300 mM of ferrozine dissolved in 0.1 M of ammonium acetate. These solutions are allowed to sit overnight and the absorbance of a given solution at 562 nm is recorded.

### 2.5. APTES and PEG-diacid (600) functionalization

Si NTs were immersed in 1% (3-aminopropyl)triethoxysilane (APTES) solution for 4 h in acetone, followed by rinsing with deionized (DI) water. Poly(ethylene glycol) diacid 600 (PEG-diacid 600) functionalization is achieved using APTES-functionalized Si NTs. This procedure involves the preparation of a solution of PEG-diacid (600) (3.3 mmol), 1-ethyl-3-(3-dimethylaminopropyl) carbodiimide (1 mmol) and N-hydroxysuccinimide (1 mmol) in 2 ml of DI water. This mixture is stirred for 15 min. Then APTES-Si NTs was added (0.8 mg) and stirred for 3 h. The product was dialysed against DI water by changing the DI water several times. The samples were stored in solution at room temperature for further use.

## 3. Results and discussion

### 3.1. Structural and morphological characterization

Transmission electron microscopy (TEM) analysis (JEOL JEM-2100) confirms that the  $\text{Fe}_3\text{O}_4$  NPs used in these experiments are uniformly spherical (figure 2) and have narrow size distributions of  $5.10 \pm 0.98\text{ nm}$  and  $8.15 \pm 1.76\text{ nm}$  (for associated histograms see the electronic supplementary material, figure S1). High-resolution TEM analysis confirms that each particle consists of well-oriented single domains with the measured distance between two adjacent lattice fringes of a value of 0.258 nm (electronic supplementary material, figure S2), close to the reported value of 0.253 nm (corresponding to the lattice spacing associated with the (311) planes of  $\text{Fe}_3\text{O}_4$ ), thereby supporting the presence of the magnetite structure.

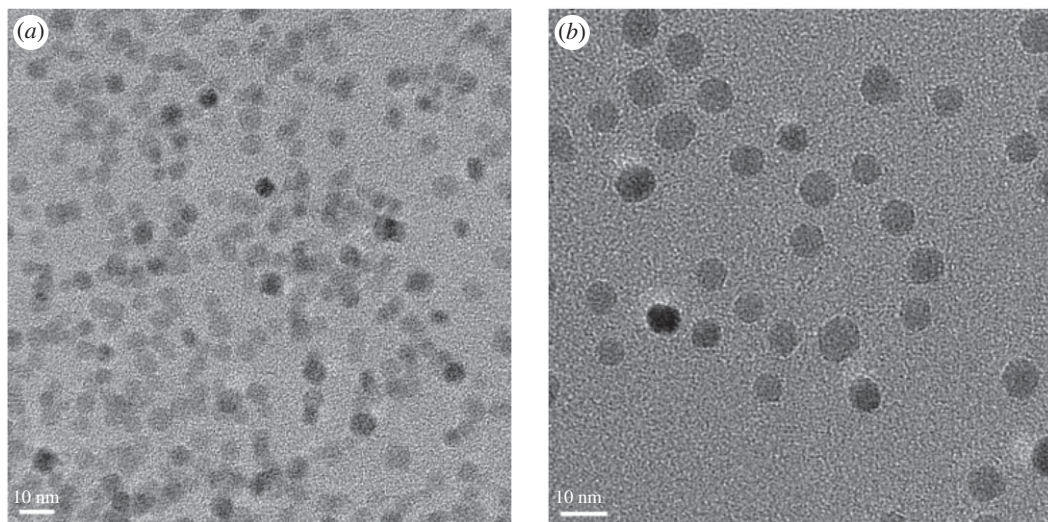


**Figure 2.** TEM images of  $\text{Fe}_3\text{O}_4$  NPs of (a) 5 nm average diameter and (b) 8 nm average diameter.

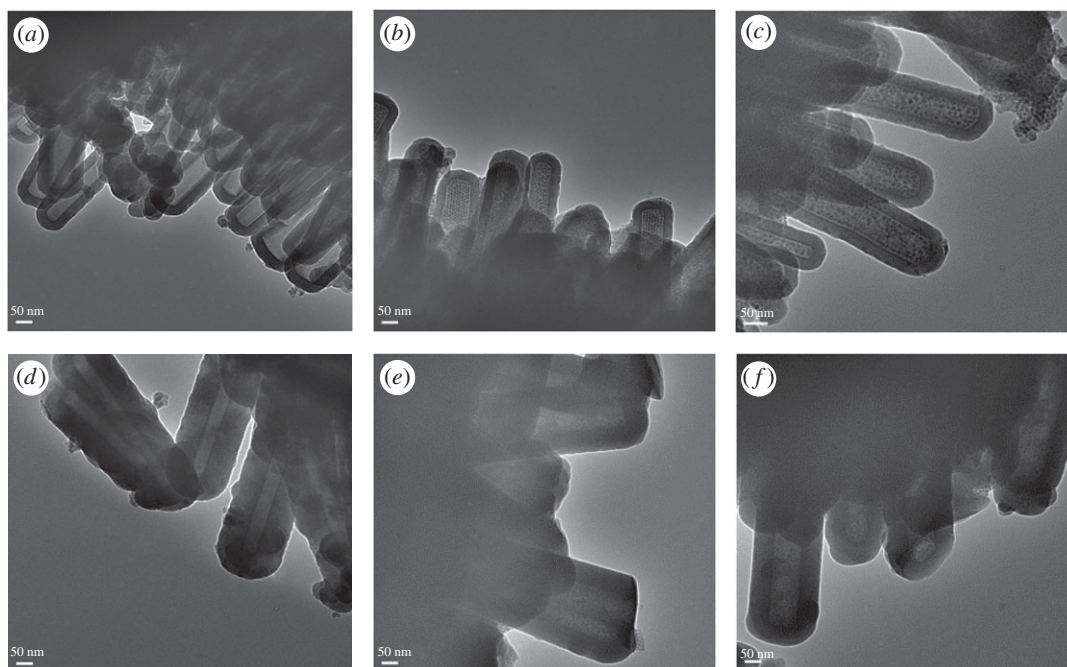


**Figure 3.** (a–c) TEM imaging of 40 nm Si NTs: (a) empty Si NTs; (b) Si NTs loaded with 5 nm  $\text{Fe}_3\text{O}_4$ ; (c) Si NTs loaded with 8 nm  $\text{Fe}_3\text{O}_4$ . (d–f) TEM of 70 nm Si NTs: (d) empty Si NTs; (e) Si NTs loaded with 5 nm  $\text{Fe}_3\text{O}_4$ ; (f) Si NTs loaded with 8 nm  $\text{Fe}_3\text{O}_4$ .

Si NTs offer a uniform wall structure and relatively large interior loading capacity, with a separation distance of magnetic NPs between tube interiors that is effectively two times the wall thickness of a given type of Si NT. TEM also confirms the successful loading of  $\text{Fe}_3\text{O}_4$  NPs into the Si NTs. Figure 3a shows empty Si NTs with a wall thickness of 40 nm; figure 3b,c shows these Si NTs loaded with  $\text{Fe}_3\text{O}_4$  NPs of 5 nm and 8 nm, respectively. In figure 3d, empty Si NTs with a wall thickness of 70 nm are presented, with figure 3e,f presenting these Si NTs loaded with 5 nm and 8 nm  $\text{Fe}_3\text{O}_4$  NPs, respectively. We observe a uniform filling of  $\text{Fe}_3\text{O}_4$  NPs inside a given Si NT. No  $\text{Fe}_3\text{O}_4$  NPs are observed outside these Si NTs, meaning that the washing process was successful, with no significant amount of  $\text{Fe}_3\text{O}_4$  NPs removed from inside the Si NTs.

It should also be pointed out that under high magnification conditions, lattice planes of  $\text{Fe}_3\text{O}_4$  NPs can be imaged inside the NTs, confirming the presence of the magnetite structures at this location. The

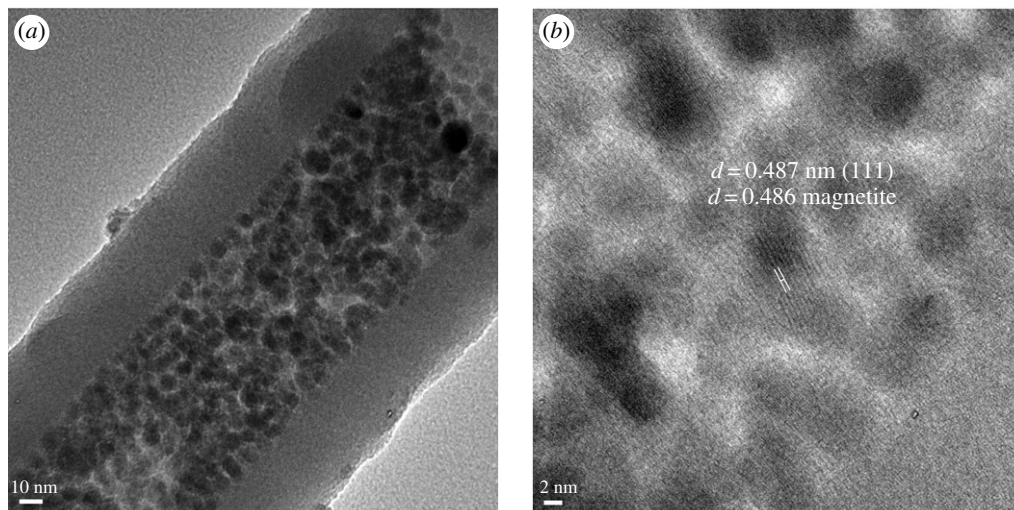


**Figure 4.** (a)  $\text{Fe}_3\text{O}_4$  NPs (8 nm average diameter) loaded into 40 nm wall thick Si NTs; (b) high-resolution TEM imaging of this sample, showing {111} spacings associated with the magnetite phase.

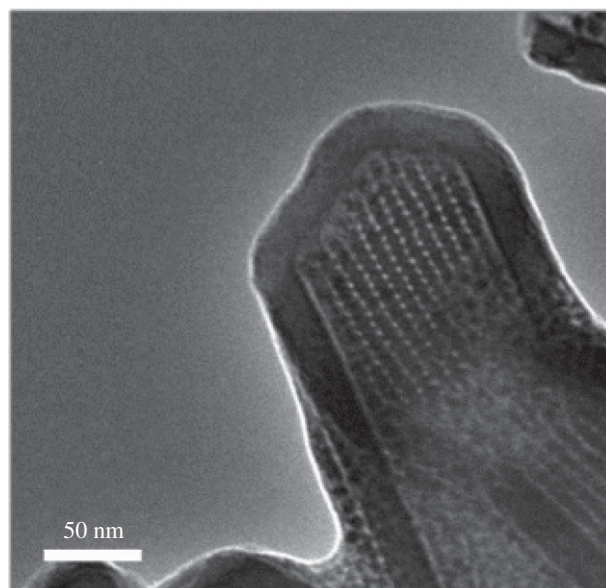


**Figure 5.** Si NT loaded with  $\text{Fe}_3\text{O}_4$  NPs, illustrating the closest packing of the nanocrystals inside the tube.

lattice spacing of the plane of the magnetite phase can be readily confirmed (figure 4a). Interestingly, in selected NTs a closest packed arrangement of  $\text{Fe}_3\text{O}_4$  NPs can also be observed (figure 5).

### 3.2. Magnetic characterization

To evaluate the potential use of this new material as an MRI contrast agent, we measured the  $T_1$  and  $T_2$  values of a given sample using a relaxometer (Bruker Minispec mq60) at 1.41 T.  $T_1$  and  $T_2$  values were recorded in phosphate buffered saline (PBS) at 37°C. A linear dependence is observed between the inverse proton relaxation times and the iron concentration according to the following equation:

$$\frac{1}{T_{i,\text{obs}}} = \frac{1}{T_{i,0}} + r_i[\text{Fe}], \quad (3.1)$$

where  $1/T_{i,\text{obs}}$  ( $i=1, 2$ ) is the inverse relaxation time measured experimentally in the presence of the magnetic nanomaterial,  $1/T_{i,0}$  is the inverse relaxation time of pure water in the absence of the

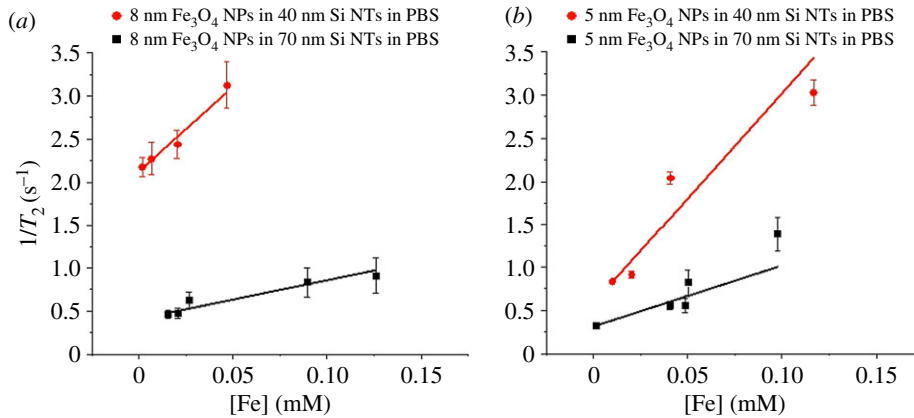


**Figure 6.**  $1/T_2$  versus  $[Fe]$  of Si NTs loaded with: (a) 8 nm  $Fe_3O_4$  NPs and (b) 5 nm  $Fe_3O_4$  NPs.

**Table 1.**  $r_1$ ,  $r_2$  and  $r_2/r_1$  values associated with  $Fe_3O_4$  NPs loaded into different Si NTs.

5 nm $Fe_3O_4$ in:	$r_1$ ( $mM^{-1} s^{-1}$ )	$r_2$ ( $mM^{-1} s^{-1}$ )	$r_2/r_1$	8 nm $Fe_3O_4$ in:	$r_1$ ( $mM^{-1} s^{-1}$ )	$r_2$ ( $mM^{-1} s^{-1}$ )	$r_2/r_1$
40 nm wall Si NTs	0.15	20.59	138.16	40 nm wall Si NTs	0.62	21.05	35.04
70 nm wall Si NTs	0.37	11.31	30.32	70 nm wall Si NTs	0.31	3.96	12.93

contrast agent,  $[Fe]$  is the iron concentration in the contrast agent and  $r_i$  is the longitudinal ( $i=1$ ) or transverse ( $i=2$ ) relaxivity (i.e. proton relaxation rate enhancement per mM Fe cation concentration) [29]. Representative plots are shown in figure 6 for  $1/T_2$  versus iron concentration for all  $Fe_3O_4$  NPs housed within Si NTs. Similar plots were undertaken for  $1/T_1$  (see the electronic supplementary material, figure S3). From linear fits of the plots,  $r_1$  and  $r_2$  can be calculated from the slopes. These  $r_1$  and  $r_2$  values are shown in table 1, as well as the corresponding  $r_2/r_1$  values. As expected,  $r_2/r_1 > 2$  is consistent with the classification of all  $Fe_3O_4$ -containing structures as a negative contrast agent. This is also true from the observation that  $r_1$  values are observed here in the range of  $0.05$ – $0.35 mM^{-1} s^{-1}$ .

Some trends emerge from a simple analysis of the measured  $r_2$  values. For all  $Fe_3O_4$  NPs loaded into Si NTs possessing 40 nm wall thickness,  $r_2$  is apparently insensitive to particle size, with a value of approximately  $21 mM^{-1} s^{-1}$ . Also, for a given  $Fe_3O_4$  NP size, we observe the fact that  $r_2$  drops a minimum of 50% with increasing wall thickness (from 40 to 70 nm).

To interpret the above trends, it is useful to examine the following size-dependent expression for  $T_2$  [30]:

$$\frac{1}{T_2} = \left( \frac{256\pi^2\gamma^2}{405} \right) \frac{V^*M_S^2a^2}{D(1+(L/a))'} \quad (3.2)$$

where  $\gamma$ , gyromagnetic ratio;  $V^*$ , volume fraction;  $a$  radius of  $Fe_3O_4$  core;  $D$  diffusivity of water molecules;  $L$ , thickness of an impermeable surface coating.

By looking at the above results, it appears that for samples in PBS, the changes in  $T_2$  values are dictated by thickness of surface coating.  $T_2$  relaxivity decreases as the Si NTs wall thickness increases, as presumably thicker Si NTs are less permeable to aqueous diffusion.

It is also informative to compare these  $r_1$  and  $r_2$  values with representative data from the existing literature. For example, Zhou obtained an  $r_1$  value for 5 nm  $Fe_3O_4$ -coated with dimercaptosuccinic acid (DMSA) of  $6.21 mM^{-1} s^{-1}$ , an  $r_2$  of  $39.53 mM^{-1} s^{-1}$  and  $r_2/r_1$  of 6.58 (at 1.5 T) [31]. Huang *et al.* reported that 5 nm  $Fe_3O_4$  coated with sodium tartrate shows an  $r_1$  of  $4.3 mM^{-1} s^{-1}$ , an  $r_2$  of  $23 mM^{-1} s^{-1}$  and  $r_2/r_1$  of 5.3 [32]. Mamor and co-workers report that 8 nm  $Fe_3O_4$  NPs coated with citric acid possesses an  $r_1$  of  $28.8 mM^{-1} s^{-1}$ , an  $r_2$  of  $54.4 mM^{-1} s^{-1}$  and  $r_2/r_1$  of 1.89 [33]. It is important to consider that in our system,  $Fe_3O_4$  NPs are not widely dispersed in the medium. Rather, all  $Fe_3O_4$  NPs are concentrated in a one-dimensional construct inside a given Si NT, but these Si NTs are well dispersed in the medium as a result of PEG (diacid) surface functionalization. Based on the data presented here, the very low values

obtained for  $r_1$  (in general, less than  $1 \text{ mM}^{-1} \text{ s}^{-1}$ ) suggests that protons in a given medium do not have facile access to the surface of the encapsulated  $\text{Fe}_3\text{O}_4$  NPs.

For this reason, it is perhaps more appropriate to compare our system with relaxometry data from  $\text{Fe}_3\text{O}_4$  clusters comprised aggregates of similar sizes of  $\text{Fe}_3\text{O}_4$  NPs previously reported [34]. Resovist<sup>®</sup>, commercially available  $\text{Fe}_3\text{O}_4$  NPs clusters coated with carboxydextran, have an overall diameter of 60 nm with an individual particle size of 4.6 nm; this cluster has an  $r_1$  of  $10.9 \text{ mM}^{-1} \text{ s}^{-1}$ , an  $r_2$  of  $190 \text{ mM}^{-1} \text{ s}^{-1}$  and  $r_2/r_1$  of 17.4 [35]. Qin *et al.* reported data for a cluster size of 71 nm with an individual particle size of 10.1 nm; this cluster is coated with Pluronic F127. These workers obtained an  $r_1$  of  $0.31 \text{ mM}^{-1} \text{ s}^{-1}$ , an  $r_2$  of  $71 \text{ mM}^{-1} \text{ s}^{-1}$  and  $r_2/r_1$  of 229 [36]. Tilborg and co-workers reported a cluster size of 62.4 nm coated with PEG2000 and an individual particle size of 9 nm. An  $r_1$  of  $0.62 \text{ mM}^{-1} \text{ s}^{-1}$ ,  $r_2$  of  $402.48 \text{ mM}^{-1} \text{ s}^{-1}$  and  $r_2/r_1$  of 647 was obtained for this system [37]. However, the extremely high value of the latter system is probably influenced by the fact that the experiments were made at 9 T versus the 1.5 T used in our experiments. It should also be noted that those clusters are spherically shaped aggregates of small spherical particles, in contrast to the rod-like structure of our NTs. However, in general, the  $r_2/r_1$  values we obtained are in the range of clusters previously reported. Most importantly, however, it is significant to note the ability of the NT wall thickness to mediate the relaxivity values (with regard to  $T_2$ ), a topic warranting further investigation and ideal expansion of the tunability of these parameters as a function of template geometry and surface chemistry.

## 4. Conclusion

This work describes a straightforward process for the incorporation of superparamagnetic  $\text{Fe}_3\text{O}_4$  NPs inside Si NTs, along with a necessary surface modification strategy for PEG functionalization. While the observed  $r_2$  values of these  $\text{Fe}_3\text{O}_4/\text{Si}$  NT composites are consistent with the clustering of  $\text{Fe}_3\text{O}_4$  NPs in the NT interior, the ability to achieve ordered closest packed nanocrystal arrays is a unique attribute of this system. Further detailed evaluation of the ability of these materials to act as a negative contrast agent *in vivo* remain.

Data accessibility. Datasets are deposited at Dryad: (<http://dx.doi.org/10.5061/dryad.k2vh732>) [38].

Authors' contributions. R.G.-R. and J.L.C. designed the experiments; R.G.-R. carried out the experiments; all authors participated in the analysis of the results and assisted with construction of the manuscript.

Competing interests. The authors declare no competing interests.

Funding. This work has been supported by a grant from the Robert A. Welch Foundation (grant no. P-1212).

Acknowledgement. The authors thank Dr Puerto Morales for the generous supply of iron oxide nanoparticles.

## References

- Moghaddam MM, Pieber B, Glasnov T, Kappe CO. 2014 Immobilized iron oxide nanoparticles as stable and reusable catalysts for hydrazine-mediated nitro reductions in continuous flow. *ChemSusChem* **7**, 3122–3131. (doi:10.1002/cssc.201402455)
- Wilhelm C, Gazeau F. 2008 Universal cell labelling with anionic magnetic nanoparticles. *Biomaterials* **29**, 3161–3174. (doi:10.1016/j.biomaterials.2008.04.016)
- Perez JM, Josephson L, Weissleder R. 2004 Use of magnetic nanoparticles as nanosensors to probe for molecular interactions. *ChemBioChem* **5**, 261–264. (doi:10.1002/cbic.200300730)
- Estelrich J, Escibano E, Queralt J, Busquets M. 2015 Iron oxide nanoparticles for magnetically-guided and magnetically-responsive drug delivery. *Int. J. Mol. Sci.* **16**, 8070–8101. (doi:10.3390/ijms16048070)
- Bañobre-López M, Teijeiro A, Rivas J. 2013 Magnetic nanoparticle-based hyperthermia for cancer treatment. *Rep. Pract. Oncol. Radiother.* **18**, 397–400. (doi:10.1016/j.rpor.2013.09.011)
- Li L, Jiang W, Luo K, Song H, Lan F, Wu Y, Gu Z. 2013 Superparamagnetic iron oxide nanoparticles as MRI contrast agents for non-invasive stem cell labeling and tracking. *Theranostics* **3**, 595–615. (doi:10.7150/thno.5366)
- Soenen SJ, De Cuyper M, De Smedt SC, Braeckmans K. 2012 Investigating the toxic effects of iron oxide nanoparticles. In *Methods enzymology* (ed. N Düzgüneş), pp. 195–224. San Diego, CA: Academic Press.
- Mahmoudi M, Simchi A, Milani AS, Stroeve P. 2009 Cell toxicity of superparamagnetic iron oxide nanoparticles. *J. Colloid Interface Sci.* **336**, 510–518. (doi:10.1016/j.jcis.2009.04.046)
- Arteaga-Cardona F, Rojas-Rojas K, Costo R, Mendez-Rojas MA, Hernando A, De La Presa P. 2016 Improving the magnetic heating by disaggregating nanoparticles. *J. Alloys Compd* **663**, 636–644. (doi:10.1016/j.jallcom.2015.10.285)
- Campbell JL, Arora J, Cowell SF, Garg A, Eu P, Bhargava SK, Bansal V, Wang Y. 2011 Quasi-cubic magnetite/silica core-shell nanoparticles as enhanced MRI contrast agents for cancer imaging. *PLoS ONE* **6**, e21857. (doi:10.1371/journal.pone.0021857)
- Arteaga-Cardona F *et al.* 2016 Cell viability and MRI performance of highly efficient polyol-coated magnetic nanoparticles. *J. Nanopart. Res.* **18**, 1–9. (doi:10.1007/s11051-016-3646-0)
- Cardona FA *et al.* 2016 Enhanced magnetic properties and MRI performance of bi-magnetic core-shell nanoparticles. *RSC Adv.* **6**, 77 558–77 568. (doi:10.1039/C6ra14265F)
- Arteaga-Cardona F, Santillán-Urquiza E, Pal U, Méndez-Alvarez ME, Torres-Duarte C, Cherr GN, de la Presa P, Méndez-Rojas MÁ. 2017 Unusual variation of blocking temperature in bi-magnetic nanoparticles. *J. Magn. Mater.* **441**, 417–423. (doi:10.1016/j.jmmm.2017.06.024)
- Santos H, Bimbo L, Herranz B, Shahbazi M, Hirvonen J, Salonen J. 2013 Nanostructured porous silicon in preclinical imaging: moving from bench to bedside. *J. Mater. Res.* **28**, 152–164. (doi:10.1557/jmr.2012.271)
- Huang X, Gonzalez-Rodriguez R, Rich R, Gryczynski Z, Coffer JL. 2013 Fabrication and size dependent

- properties of porous silicon nanotube arrays. *Chem. Comm.* **49**, 5760–5762. (doi:10.1039/C3CC41913D)
17. Bjørnerud A, Johansson LO, Briley-Sæbø K, Ahlström HK. 2002 Assessment of T1 and T<sub>2</sub> effects *in vivo* and *ex vivo* using iron oxide nanoparticles in steady state—dependence on blood volume and water exchange. *Magn. Reson. Med.* **47**, 461–471. (doi:10.1002/mrm.10066)
  18. Hu F, Zhao YS. 2012 Inorganic nanoparticle-based T<sub>1</sub> and T<sub>1</sub>/T<sub>2</sub> magnetic resonance contrast probes. *Nanoscale* **4**, 6235–6243. (doi:10.1039/C2NR31865B)
  19. Kim BH *et al.* 2011 Large-scale synthesis of uniform and extremely small-sized iron oxide nanoparticles for high-resolution T1 magnetic resonance imaging contrast agents. *J. Am. Chem. Soc.* **133**, 12 624–12 631. (doi:10.1021/ja203340u)
  20. Hurley KR, Lin Y-S, Zhang J, Egger SM, Haynes CL. 2013 Effects of mesoporous silica coating and postsynthetic treatment on the transverse relaxivity of iron oxide nanoparticles. *Chem. Mater.* **25**, 1968–1978. (doi:10.1021/cm400711h)
  21. Bae H, Ahmad T, Rhee I, Chang Y, Jin S-U, Hong S. 2012 Carbon-coated iron oxide nanoparticles as contrast agents in magnetic resonance imaging. *Nanoscale Res. Lett.* **7**, 44. (doi:10.1186/1556-276x-7-44)
  22. Mou X, Wei X, Li Y, Shen W. 2012 Tuning crystal-phase and shape of Fe<sub>2</sub>O<sub>3</sub> nanoparticles for catalytic applications. *CrystEngComm* **14**, 5107–5120. (doi:10.1039/C2CE25109D)
  23. Schmidtke C *et al.* 2014 Polymer-assisted self-assembly of superparamagnetic iron oxide nanoparticles into well-defined clusters: controlling the collective magnetic properties. *Langmuir* **30**, 11 190–11 196. (doi:10.1021/la5021934)
  24. Liu X *et al.* 2014 Design of covalently functionalized carbon nanotubes filled with metal oxide nanoparticles for imaging, therapy, and magnetic manipulation. *ACS Nano* **8**, 11 290–11 304. (doi:10.1021/nn5040923)
  25. Baaziz W *et al.* 2013 Carbon nanotube channels selectively filled with monodispersed Fe<sub>3</sub>-xO<sub>4</sub> nanoparticles. *J. Mater. Chem. A* **1**, 13 853–13 861. (doi:10.1039/C3TA12734F)
  26. Granitzer P, Rumpf K, Gonzalez-Rodriguez R, Coffey JL, Reissner M. 2015 The effect of nanocrystalline silicon host on magnetic properties of encapsulated iron oxide nanoparticles. *Nanoscale* **7**, 20 220–20 226. (doi:10.1039/C5NR05232G)
  27. Granitzer P, Rumpf K, Gonzalez R, Coffey J, Reissner M. 2014 Magnetic properties of superparamagnetic nanoparticles loaded into silicon nanotubes. *Nanoscale Res. Lett.* **9**, 413. (doi:10.1186/1556-276x-9-413)
  28. Riemer J, Hoepken HH, Czerwinska H, Robinson SR, Dringen R. 2004 Colorimetric ferrozine-based assay for the quantitation of iron in cultured cells. *Anal. Biochem.* **331**, 370–375. (doi:10.1016/j.ab.2004.03.049)
  29. Pereira C, Pereira AM, Rocha M, Freire C, Geraldes CFGC. 2015 Architected design of superparamagnetic Fe<sub>3</sub>O<sub>4</sub> nanoparticles for application as MRI contrast agents: mastering size and magnetism for enhanced relaxivity. *J. Mater. Chem. B* **3**, 6261–6273. (doi:10.1039/C5TB00789E)
  30. Tong S, Hou S, Zheng Z, Zhou J, Bao G. 2010 Coating optimization of superparamagnetic iron oxide nanoparticles for high T<sub>2</sub> relaxivity. *Nano Lett.* **10**, 4607–4613. (doi:10.1021/nl102623x)
  31. Zhou Z, Zhao Z, Zhang H, Wang Z, Chen X, Wang R, Chen Z, Gao J. 2014 Interplay between longitudinal and transverse contrasts in Fe<sub>3</sub>O<sub>4</sub> nanoplates with (111) exposed surfaces. *ACS Nano* **8**, 7976–7985. (doi:10.1021/nn5038652)
  32. Huang J, Wang L, Lin R, Wang AY, Yang L, Kuang M, Qian W, Mao H. 2013 Casein-coated iron oxide nanoparticles for high MRI contrast enhancement and efficient cell targeting. *ACS Appl. Mater. Interfaces* **5**, 4632–4639. (doi:10.1021/am400713j)
  33. Hatakeyama M *et al.* 2011 A two-step ligand exchange reaction generates highly water-dispersed magnetic nanoparticles for biomedical applications. *J. Mater. Chem.* **21**, 5959–5966. (doi:10.1039/C1JM04381H)
  34. Paquet C, de Haan HW, Leek DM, Lin H-Y, Xiang B, Tian G, Kell A, Simard B. 2011 Clusters of superparamagnetic iron oxide nanoparticles encapsulated in a hydrogel: a particle architecture generating a synergistic enhancement of the T<sub>2</sub> relaxation. *ACS Nano* **5**, 3104–3112. (doi:10.1021/nn2002272)
  35. Kim HM, Lee H, Hong KS, Cho MY, Sung M-H, Poo H, Lim YT. 2011 Synthesis and high performance of magnetofluorescent polyelectrolyte nanocomposites as MR/near-infrared multimodal cellular imaging nanoprobe. *ACS Nano* **5**, 8230–8240. (doi:10.1021/nn202912b)
  36. Qin J, Laurent S, Jo YS, Roch A, Mikhaylova M, Bhujwala ZM, Muller RN, Muhammed M. 2007 A high-performance magnetic resonance imaging T<sub>2</sub> contrast agent. *Adv. Mater.* **19**, 1874–1878. (doi:10.1002/adma.200602326)
  37. Cormode DP *et al.* 2011 A versatile and tunable coating strategy allows control of nanocrystal delivery to cell types in the liver. *Bioconjug. Chem.* **22**, 353–361. (doi:10.1021/bc1003179)
  38. Gonzalez-Rodriguez R, Granitzer P, Rumpf K, Coffey JL. 2018 Data from: New MRI contrast agents based on silicon nanotubes loaded with superparamagnetic iron oxide nanoparticles. Dryad Digital Repository. (<http://dx.doi.org/10.5061/dryad.k2vh732>)